photonics

MDPI

Article

Fluorescent Microscopy of Hot Spots Induced by Laser Heating of Iron Oxide Nanoparticles

Anastasia Ryabova [1,2,*], Daria Pominova [1,2], Inessa Markova [2], Aleksey Nikitin [3], Petr Ostroverkhov [4], Polina Lasareva [5], Alevtina Semkina [5], Ekaterina Plotnikova [4,6], Natalia Morozova [6], Igor Romanishkin [1], Kirill Linkov [1], Maksim Abakumov [3], Andrey Pankratov [4,6], Rudolf Steiner [2] and Victor Loschenov [1,2]

1 Prokhorov General Physics Institute of the Russian Academy of Sciences, 119991 Moscow, Russia; pominovadv@nsc.gpi.ru (D.P.); igor.romanishkin@nsc.gpi.ru (I.R.); kir@nsc.gpi.ru (K.L.); loschenov@nsc.gpi.ru (V.L.)
2 Department of Laser Micro-Nano and Biotechnologies, Engineering Physics Institute of Biomedicine, National Research Nuclear University MEPHI, 115409 Moscow, Russia; miv008@campus.mephi.ru (I.M.); rudolf.steiner@ilm-ulm.de (R.S.)
3 Biomedical Nanomaterials Laboratory, National University of Science and Technology "MISIS", 119049 Moscow, Russia; nikitin.aa@misis.ru (A.N.); abakumov.ma@misis.ru (M.A.)
4 Lomonosov Institute of Fine Chemical Technologies, Russian Technological University MIREA, 119454 Moscow, Russia; ostroverhov@mirea.ru (P.O.); plotnikovaekaterina62@gmail.com (E.P.); andreimnioi@yandex.ru (A.P.)
5 Department of Medical Nanobiotechnology, Pirogov Russian National Research Medical University, 117997 Moscow, Russia; polizara604@gmail.com (P.L.); semkina_as@rsmu.ru (A.S.)
6 Department of Experimental Pharmacology and Toxicology, National Medical Research Radiological Centre of the Ministry of Health of the Russian Federation, Hertsen Moscow Oncology Research Institute, 125284 Moscow, Russia; n.b.morozova@yandex.ru
* Correspondence: nastya.ryabova@nsc.gpi.ru; Tel.: +7-(499)-503-87-77 (ext. 1-11)

Abstract: Determination of the iron oxide nanoparticles (IONPs) local temperature during laser heating is important in the aspect of laser phototherapy. We have carried out theoretical modeling of IONPs local electromagnetic (EM) field enhancement and heating under the laser action near individual IONPs and ensembles of IONPs with different sizes, shapes and chemical phases. For experimental determination of IONPs temperature, we used fluorescence thermometry with rhodamine B (RhB) based on its lifetime. Depending on the IONPs shape and their location in space, a significant change in the spatial distribution of the EM field near the IONPs surface is observed. The local heating of IONPs in an ensemble reaches sufficiently high values; the relative change is about 35 °C for Fe_2O_3 NPs. Nevertheless, all the studied IONPs water colloids showed heating by no more than 10 °C. The heating temperature of the ensemble depends on the thermal conductivity of the medium, on which the heat dissipation depends. During laser scanning of a cell culture incubated with different types of IONPs, the temperature increase, estimated from the shortening of the RhB fluorescence lifetime, reaches more than 100 °C. Such "hot spots" within lysosomes, where IONPs predominantly reside, lead to severe cellular stress and can be used for cell therapy.

Keywords: iron oxide nanoparticles; laser induced heating; local field enhancement; fluorescent thermometry

check for updates

Citation: Ryabova, A.; Pominova, D.; Markova, I.; Nikitin, A.; Ostroverkhov, P.; Lasareva, P.; Semkina, A.; Plotnikova, E.; Morozova, N.; Romanishkin, I.; et al. Fluorescent Microscopy of Hot Spots Induced by Laser Heating of Iron Oxide Nanoparticles. *Photonics* **2023**, *10*, 705. https://doi.org/10.3390/photonics10070705

Received: 5 May 2023
Revised: 14 June 2023
Accepted: 19 June 2023
Published: 21 June 2023

Copyright: © 2023 by the authors. Licensee MDPI, Basel, Switzerland. This article is an open access article distributed under the terms and conditions of the Creative Commons Attribution (CC BY) license (https://creativecommons.org/licenses/by/4.0/).

1. Introduction

IONPs are promising for diagnostics as magnetic resonance imaging (MRI) contrast agents, and for therapy: they can be coated with a photosensitizer for photodynamic therapy, and laser or magnetic heating of IONPs can be used for controlled drug release or phototherapy [1].

Magnetic or plasmon resonance nanoparticles (NPs) are increasingly being used to localize the process of hyperthermia [2] and to increase the selectivity of therapeutic action.

Resonant nanostructures, so-called nanoantennas, are known to control the electrical and magnetic components of the optical wave on the nanometer scale: they convert freely propagating EM waves into a near-field and multiply the field intensity in the subwavelength range [3–5]. The most commonly used nanoantennas made of noble metals, also called plasmonic, which provide strong localization of the exciting EM field on the scale of about 100 nm due to the occurrence of localized plasmon resonance [6]. There is a growing interest in hybrid and dielectric nanoantennas made of materials with high refractive index [7]. Dielectric nanoantennas possess both electric and magnetic Mie resonances [8,9], since the EM field can freely penetrate inside the dielectric nanostructures. The degree of field localization and the local field enhancement factor for dielectric nanoantennas are lower than for plasmonic nanoantennas; however, by optimizing the shape of NPs and by using dimers and trimers consisting of two or three NPs, better field localization near NPs can be achieved.

In semiconducting materials, such as iron oxides, the energy of optical radiation allows the temporary transition of electrons from the valence band to the conduction band, which leads to heat release as the electrons relax back to the valence band [10]. At the same time, the photothermal conversion of nonmetallic inorganic NPs demonstrates a more moderate efficiency than that of their metallic counterparts [7,11].

As a result of EM field localization and photothermal transformation, the so-called "hot spots" can arise near the aggregates of NPs. The distribution of "hot spots" at the nano- and microscale determines the thermal response of the entire sample.

In the case of magnetic hyperthermia, the times of Brownian, Neel and effective relaxations as a function of particle diameter for different values of the anisotropy constant have been studied in detail [12]. In magnetic hyperthermia, the intracellular aggregation of IONPs within endosomes is recognized as an important problem because it suppresses both physical mechanisms that explain heat release: the Brownian relaxation of NPs and the Neel relaxation [13]. More recently, IONPs have been tested for photothermal therapy in vitro and in vivo [14]. The use of iron oxide nanocubes as sensors of both magnetic and laser hyperthermia simultaneously to perform dual mode hyperthermia has shown the effectiveness of hyperthermia leading to cell death in mouse tumor models [15]. The effect of laser hyperthermia was demonstrated on magnetic IONPs coated with the IR dyes Cyanine7 [16] and IR-780 [17]. It was observed that intracellular aggregation of IONPs in vesicles leads to an increase in photothermal heating of the NPs and cell death by hyperthermia (10 min of irradiation at 1064 nm with a power density of 300 mW/cm^2) [18].

Works demonstrating the successful use of IONPs in combination with photosensitizers for photodynamic therapy are appearing [19,20].

Previously, we demonstrated a sparking effect during laser scanning of cell culture samples with IONPs [21]. It was shown that IONPs accumulate in cell lysosomes, and during laser scanning bright flashes are observed in the area of lysosomes, whose spectrum corresponds to the black body emission spectrum, which may indicate a high heating temperature and thermal luminescence.

Measuring the temperature of NP-containing cell organelles during laser heating is a complex and challenging technique. Fluorescence thermometers are reliable tools for measuring temperature fluctuations in nano-volumes because of their advantages such as fast response, high sensitivity and spatial resolution, ease of use and non-destructive detection [22].

For example, RhB is used in laser-induced fluorescence thermometry due to the property that the quantum yield of emission decreases with increasing temperature, which is a consequence of the rotation of diethylamine groups on the xanthene ring. The fluorescence lifetime of RhB depends on the local environment (temperature, pH, charge, etc.) but is independent of dye concentration, excitation efficiency, or detection efficiency [23]. In biological samples, RhB was found to be generally non-toxic at low concentrations, around 40 nM [24]. In general, RhB localizes inside mitochondria when accumulated within cells [25,26]. Fluorescence thermosensors based on RhB have been developed in

the form of functional polymer microparticles [27,28] and in the form of RhB molecular solutions [29] for in vivo applications.

In this work, an experimental study of the formation of "hot spots" of ensembles of IONPs of different sizes and shapes during laser scanning with the estimation of the heat distribution over the cell volume using the fluorescent RhB thermosensor was carried out. In order to interpret the experimental data obtained, numerical simulations of the scattering and absorption cross sections of the studied IONPs and their ensembles, as well as of the field enhancement and heating during the interaction with the excitation EM radiation were performed using the finite-difference time-domain method.

2. Materials and Methods

2.1. Materials

Iron (III) acetylacetonate ($Fe(acac)_3$, 99%), 1,2-hexadecanediol (1,2-HDD, 90%), cyclopropanecarboxylic acid (95%), benzyl alcohol (99.8%), benzyl ether (98%), oleic acid (OA, 90%), oleylamine (OAm, 70%), iron (III) chloride ($FeCl_3$; ≥98%), polyethyleneimine (PEI, Mw = 25 kDa, Mn = 10 kDa), biphenyl-4-carboxylic acid (95%), cobalt (II) acetylacetonate ($Co(AcAc)_2$, 97%), 3,4-dihydroxyphenylacetic acid (DOPAC, 98%), bovine serum albumin, glutaraldehyde 25% (w/v) aqueous solution, N-hydroxysuccinimide (NHS), 1-ethyl-3-(3-dimethylaminopropyl) carbodiimide (EDC), sodium borohydride ($NaBH_4$), 2-propanol, hexane, methanol, ethanol and toluene were purchased from Sigma-Aldrich (St. Louis, MA, USA). Acetone (99.5%, ChimMed, Moscow, Russia), human serum albumin (HSA, Microgen, Moscow, Russia), RhB (SSC NIOPIK, Moscow, Russia), monoamino terminated poly(ethylene glycol) hydrochloride (2 kDa, PEG-NH_2, Creative PEGWorks, Durham, NC, USA) were used. Two types of commercially available IONPs were used in the work: γ-Fe_2O_3 NanoArc® [30] (Alfa Aesar, Kandel, Germany) and pharmaceutical preparation Ferinject® [31] (Vifor Pharma, St. Gallen, Switzerland).

2.2. IONPs Synthesis

To experimentally change the temperature of colloids of IONPs, we used IONPs in the form of spheres, spherical clusters, cubes, rods and octopodes of various sizes of the magnetic core and different chemical compositions in them.

Spherical HSA-coated Fe_2O_3 NPs (cores 6 ± 2 nm, hydrodynamic diameter of clusters 37.28 ± 0.11 nm, average number of magnetic cores in a cluster 4 ± 2) were prepared according to [32]. Briefly, magnetic cores were produced by thermal decomposition of $Fe(acac)_3$ (30 mmol) in benzyl alcohol (220 mL). After magnetic cores (80 mg) were covered with HSA (0,8 mL, 20%) and ε-NH_2 groups were cross-linked with glutaric aldehyde (920 mkl, 25%) followed by $NaBH_4$ (0.35 mmol) reduction. In the final step, carboxyl groups from protein were linked with NH_2-PEG-OH. Unbound PEG was removed from NPs by gel filtration using a PD-10 column (Sepadex G25, Sigma-Aldrich, St. Louis, MO, USA, eluent—phosphate-buffered saline).

OA-capped Fe_3O_4 spherical cluster-like NPs (35 ± 7 nm) were synthesized according to [31]. Briefly, the mixture of 2 mmol of $Fe(acac)_3$, 8 mmol of 1,2-HDD, 6 mmol of cyclopropanecarboxylic acid in benzyl ether (20 mL) was placed in a 250 mL three-necked round bottom flask, equipped with a reflux condenser and thermometer. Then, the mixture was heated to 210 °C at a rate of about 5 °C/min and held at this temperature for 1 h. Then, the temperature was raised to 260 °C with a rate of 5 °C/min and held at this temperature for 30 min. NPs were collected by centrifugation at 6000 rpm, 30 min after the addition of 10 mL of 2-propanol-hexane mixture (v/v = 1/1). Finally, the NPs were redispersed in toluene.

OA-capped cubic Fe_3O_4 NPs (15 ± 4 nm) were synthesized as follows. 0.5 mmol of $Fe(acac)_3$, 4 mmol of 1,2-HDD, 2 mmol of OAm, 10 mmol of OA, and 20 mL of benzyl ether were mixed together in a three-necked round bottom flask and heated to boiling point at a rate of 3 °C/min under argon flow and vigorous stirring. The mixture was boiled for

2 h followed by removal of the heat source. The NPs were separated by centrifugation at 6000 rpm after addition of ethanol (5 mL) and hexane (5 mL) and redispersed in toluene.

OA-capped cubic Fe_3O_4 NPs (37 ± 6 nm) were synthesized according to the [33]. Briefly, 1 mmol $Fe(acac)_3$, 8 mmol of 1,2-HDD, 4 mmol of OAm and 20 mL of benzyl ether were mixed together in a three-necked round bottom flask and heated to boiling point at a rate of 3 °C/min under argon flow and vigorous stirring. The mixture was boiled for 2 h followed by removal of the heat source. The NPs were separated by centrifugation at 6000 rpm after addition of ethanol (5 mL) and hexane (5 mL) and redispersed in toluene.

OA-capped octopod-like Fe_3O_4 NPs (14 ± 2 nm) were synthesized by thermal decomposition technique. The mixture of 2 mmol of $Fe(acac)_3$, 6 mmol of OA, 6 mmol of biphenyl-4-carboxylic acid in benzyl ether (20 mL) was placed in a 250 mL three-necked round bottom flask equipped with a reflux condenser and a thermometer. The mixture was then heated to 210 °C at a rate of about 5 °C/min and held at this temperature for 1 h. Then, the temperature was raised to 260 °C at a rate of 5 °C/min and maintained for 30 min. NPs were collected by centrifugation (6000 rpm, 30 min) after adding 10 mL of 2-propanol-hexane mixture (v/v = 1/1). Finally, NPs were redispersed in toluene.

OA-capped octopod-like $CoFe_2O_4$ NPs (31 ± 4 nm) were synthesized by thermal decomposition technique. The mixture of 2 mmol of $Fe(acac)_3$, 1 mmol of $Co(acac)_2$, 8 mmol of OA, 2 mmol of OAm and 40 mL of benzyl ether was placed was paced in a 250 mL three-necked round bottom flask equipped with a reflux condenser and a thermometer. The mixture was heated up to 280 °C at a rate of 3 °C/min under argon flow and kept for another 2 h. After cooling the solution to room temperature, NPs were separated from the solution by centrifugation for 30 min at 6000 rpm, after which the formed precipitate was dispersed in toluene.

Hydrophilization of OA-capped spherical cluster-like, octopod-like and cubic NPs was performed using DOPAC as described in [34]. Surface modification of NPs with DOPAC. The mixture of 24 mg of NaOH and 51 mg of DOPAC was dissolved in 10 mL of methanol. Then, 10 mL of NPs in toluene ([Fe] = 0.5 mg/mL) were added to the prepared mixture, followed by the incubation for 5 h at 50 °C under vigorous stirring. After cooling the mixture to room temperature, the modified NPs were separated from the supernatant by centrifugation at 6000 rpm for 20 min and redispersed in 10 mL of deionized water. The NPs were washed three times with pure deionized water using centrifugal filters Amicon Ultra-4, MWCO 30 kDa (Millipore, Burlington, MA, USA) and separated from aggregates by passing through 0.45 syringe filter Millex-HV (Millipore, Burlington, MA, USA).

Rod-like NPs of β-FeOOH akaganeite (14 ± 4 nm length, 3 ± 1 nm diameter) were synthesized according to [35]. A solution (100 mL) containing 0,2 M $FeCl_3$ and $8{\cdot}10^{-4}$ mM PEI, was heated to 80 °C and held for 2 h. After that, NPs were separated by adjusting pH to 7.0, followed by centrifugation at 6000 rpm. The precipitate was dispersed in pure deionized water.

TEM analysis was performed using a JEM-1400 microscope (JEOL, Tokyo, Japan), 120 kV. Colloids of NPs (10 µL with [Fe] = 0.1 mg/mL) were dropped onto the surface of a Formvar-coated copper grid, followed by the evaporation of the solvent. Core size distribution analysis was performed using ImageJ software for 500 individual NPs.

XRD analysis of dried powders of NPs was performed at room temperature using an X-ray power diffractometer DRON-4 (BOUREVESTNIK, Saint-Petersburg, Russia) with Co Kα radiation. Data were collected from 2θ = 20–100° at a scan rate of 0.1° per step and 3 s per point. A qualitative phase analysis was performed by comparing the obtained spectra with PHAN database (National University of Science and Technology "MISIS", Moscow, Russia) [36].

2.3. Temperature Measuring in IONPs Water Colloids

The fluorescence lifetime of RhB was used to experimentally analyze the temperature during laser heating of the water colloids of IONPs. We used RhB at a concentration of 10 µM in distilled water. At this concentration, the fluorescence decay of RhB remained

monoexponential. A thermostat in the microscope slide (PeCon GmbH, Erbach, Germany) was used to calibrate the temperature dependence of the fluorescence lifetime of the RhB solution. The temperature range of 20–60 °C with of 5 °C intervals was used. Equilibrium was reached in approximately 5 min for each temperature point. A concentration of 10 mg/L by weight of iron was used to experimentally determine the temperature of aqueous colloids of IONPs.

Fluorescence images were recorded using an LSM-710-NLO inverted laser scanning confocal microscope (Carl Zeiss AG, Oberkochen, Germany). The fluorescence lifetime of RhB was recorded with a FLIM module (Becker & Hickl GmbH, Berlin, Germany) attached to the LSM-710-NLO, consisting of a time-correlated single photon counting (TCSPC) system SPC-150, a GaAsP HPM-100-07 hybrid photodetector, and SPCM software. RhB fluorescence excitation was performed at two-photon absorption at 840 nm with a Chameleon Ultra II femtosecond laser (Coherent, Santa Clara, CA, USA), 140 fs pulse width, 80 MHz repetition rate. Time-resolved fluorescence images were processed using SpcImage 8.0 software (Becker & Hickl GmbH, Berlin, Germany).

Laser power at the lens exit was determined using a LabMax-TO laser power meter (Coherent, Santa Clara, CA, USA). The laser power (1% of the laser power in the program) corresponded to 1 mW measured at the lens exit.

The intensity distribution of the scanning laser spot was calculated by considering the size of the area bounded by the first-order diffraction ring for the PSF_{ill} (or Airy disk) point distribution function, with radius $r = 0.61 \cdot \lambda_{exc}/NA$, where NA is the numerical aperture of the microscope objective, λ_{exc} is the wavelength of excitation light. For the 840 nm laser, 63× oil objective with NA = 1.4, r = 366 nm, spot area S = 0.421 μm^2.

The power densities when scanning with a 1 mW laser corresponded to $\rho = P/S = 0.24$ MW/cm^2. The heating of IONPs was studied in the range of excitation laser power densities from 0.24 to 2.4 MW/cm^2 in steps of 0.15 MW/cm^2.

The irradiation dose at a scan speed of 1.27 µs/pixel for a single run was 0.3 J/cm^2.

2.4. Temperature Measuring of IONPs "Hot Spots" in Cells In Vitro

Laser-scanning induced hot spots after incubation with IONPs were studied in HeLa cell culture. Cells were grown in DMEM medium (Gibco, Paisley, UK) supplemented with 10% fetal bovine serum (FBS, BioSera, Nuaille, France), 100 U/mL penicillin and 100 µg/mL streptomycin (Life Technologies, Carlsbad, CA, USA), 2 mM glutamine (Life Technologies, Carlsbad, CA, USA) and 1 mM sodium pyruvate (Life Technologies, Carlsbad, CA, USA) in standard conditions (37 °C, 5% CO_2). Cells were subcultured every third day. For confocal microscopy, cells were seeded in a POC-R2 glass-bottom Petri dish (PeCon GmbH, Erbach, Germany) at a density of 100×10^3 cell/cm^2 one day before the experiment. Twenty-four hours later, IONPs at a concentration of 10 mg/L by weight of iron and RhB at a concentration of 1 µM were added to the cells 30 min before the microscopic examination. The cells were washed three times with prewarmed phosphate-buffered saline before microscopic examination. A thermostat in the microscope slide (PeCon GmbH, Erbach, Germany) was used to calibrate the temperature determination in the cells by the fluorescence lifetime of RhB. Cells with RhB were recorded at temperatures of 20–60 °C at 5 °C intervals.

2.5. Modeling of Local Field Enhancement and Heating for IONPs Ensembles under the Action of EM Radiation

In order to interpret the experimental results and investigate the local heating of particles at the nanoscale as a result of interaction with EM radiation, finite-difference time-domain method was used [37,38]. In this method, the numerical solution of the Maxwell equation in the time domain for three-dimensional objects is carried out. The advantage of this method is a good description of the near fields near the interfaces.

A step-by-step procedure was used, including the calculation of the absorption and scattering cross sections (σ_{abs} and σ_{sca}), EM field enhancement near the surface of IONPs

(COMSOL Multiphysics module Electromagnetic Waves, Frequency Domain), and the temperature changes with respect to the ambient temperature during resonant excitation of the IONPs by an EM wave (COMSOL Multiphysics module Heat Transfer in Solids). This procedure allows calculating the response of the response of NPs for different configurations in terms of the scattering and absorption cross sections and field enhancement near the NP surface, as well as the temperature change relative to the ambient temperature during resonant excitation of NPs by an EM wave for NPs of various shapes and sizes, as well as for ensembles of NPs.

The simulation was carried out for individual cubic and spherical Fe_3O_4 NPs of 15 and 35 nm size, as well as for $5 \times 5 \times 3$ and $3 \times 3 \times 3$ NPs arrays. The distance between the particles in the array was set equal to 5 and 15 nm.

To evaluate the effect of the magnetic core material on the heating temperature, we also simulated the heating of Fe_2O_3 NPs of a cubic and shaped shape with a size of 15 nm, as well as flat "flakes" with a size of 35 nm and a thickness of 5 nm (corresponding to the NanoArc experimental sample).

The complex refractive index of iron oxide was taken from (https://refractiveindex.info/, accessed on 18 March 2021) where the data from the works [39,40] are presented, the dependence of the refractive index n and the extinction coefficient k on the wavelength, used for calculation are shown in Figure 1.

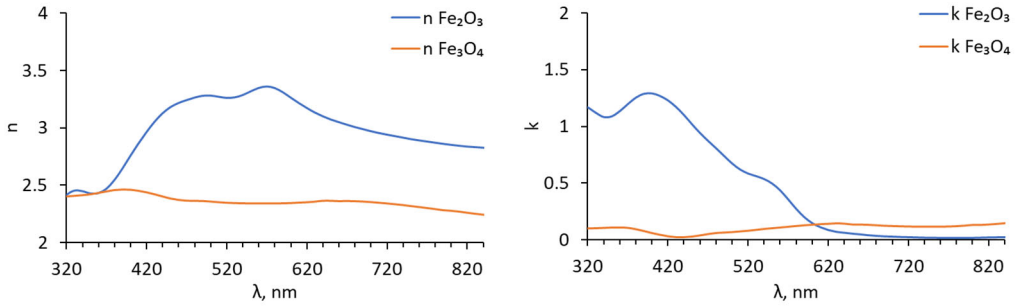


Figure 1. The dependence of the refractive index n and the extinction coefficient k on the wavelength.

The scattering and absorption cross sections were calculated in the 320–840 nm wavelength range. The calculation of the EM field spatial distribution and the local enhancement of the field between particles was carried out for wavelengths of 420 nm (two-photon excitation) and 840 nm (single-photon excitation). The light beam intensity has been evaluated as 0.24 MW/cm^2, corresponding to the laser power used in the experiments (1% of the laser power). The exposure time of the particles to EM radiation was assumed to be 1.27 µs (the time of one pixel registration).

In the calculation, the array of IONPs was assumed to be illuminated by a plane wave propagating along the z-axis and polarized along the y-axis. In the case of anisotropic NPs, the interaction with EM wave was calculated for particles oriented along the x, y and z axes and then averaged. The permittivities of the medium and the NPs were taken into account in the calculation. Water or a cell membrane was used as the surrounding dielectric medium in the model. The parameters of the materials used in the simulation are shown in Table 1.

Table 1. Parameters of the materials used in the simulation, k—thermal conductivity, ρ—density, c_p -specific heat capacity.

	k [W/m·K]	**ρ [kg/m^3]**	**c_p [J/Mol·K]**	**References**
Fe_2O_3	7	5240	104	[41,42]
Fe_3O_4	5.9	5170	104	[43]
water	0.6	1028	4182	[44]
cells	0.4	1028	4182	[45]
cell membrane	0.2	997	30	[44,46]

The field enhancement near the surface of the IONPs was estimated as the ratio of the field generated by the interaction of the NPs with an EM wave to the initial value of the field E_0.

The energy absorbed by the IONPs is then converted into heat [47], thus the NP is a source of EM heating that releases heat into the environment. The region of interaction with the EM wave was set (IONPs surfaces and the environment), it was considered that the system is at room temperature. NPs interact with EM radiation, the power absorbed by the NPs was estimated as the integrated power dissipated in the volume (i.e., total system losses) based on the calculated EM fields.

3. Results

3.1. NPs Characterization

The phase composition of the synthesized NPs was studied by XRD analysis (Figure S1). The position and relative intensity of crystal planes for all samples, except Rods 14 nm, indicate the formation of pure cubic spinel structures (space group $Fd\bar{3}m$). The XRD pattern of Rods 14 nm represents the pure tetragonal phase of akaganeite β-FeOOH (a = 10.521 Å, c = 3.030 Å, space group $I4/m$), identical to the JCPDS card #34-1266 of a standard akaganeite. The diffraction peaks of the 6 nm spherical NPs are broadened, indicating a small size of the NP crystallites, consistent with the TEM data. Based on the molar ratio Co:Fe = 1:2 determined by atomic emission spectroscopy in Octopodes-31 NPs, they can be attributed to the $CoFe_2O_4$ phase.

Since it is rather difficult to distinguish between the phases of complex ferrites, magnetite, and maghemite from the XRD data, some samples were additionally studied by Mössbauer spectroscopy. It should be noted that we have previously shown using ^{57}Fe Mössbauer spectroscopy, that 6 nm spherical NPs are maghemite (γ-Fe_2O_3), rather than magnetite (Fe_3O_4) [48]. For Spherical cluster NPs, the formation of a pure Fe_3O_4 phase was also previously shown [49]. The hyperfine magnetic structure of other samples was additionally studied by ^{57}Fe Mössbauer spectroscopy (Figure S2).

The roomtemperature Mössbauer spectrum of 37 nm Cube NPs shows the superposition of two sextets indicating the presence of Fe^{2+} and Fe^{3+} ions in two different local environments. The calculation of the sextet's parameters gives the isomer shifts IS and hyperfine magnetic field B_{hf} values: IS_1 = 0.281 ± 0.004 mm/s (B_{hf1} = 48.6 ± 0.1 T) and IS_2 = 0.662 ± 0.005 mm/s (B_{hf2} = 45.6 ± 0.1 T). These values are in good agreement with previously reported values for Fe_3O_4 NPs [50].

The NPs used in the experiments, their TEM images, and size distribution are given in Table 2.

Table 2. Size of IONPs, studied in the work.

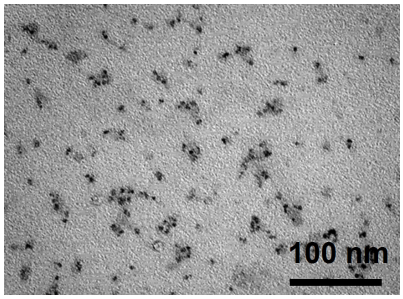
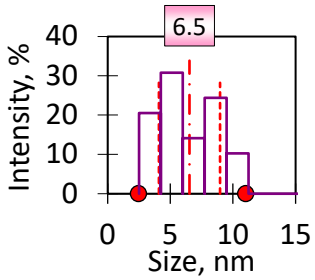
	Shape **Size of Magnetic Core [nm]** **Phase Composition**	**Microphotograph of NPs**	**Size Distribution**
1	Spheres 6 nm 6 ± 2 nm Fe_2O_3 Hydrodynamic diameter of clusters 37.28 ± 0.11 nm, average number of magnetic cores in a cluster 4 ± 2		

Table 2. *Cont.*

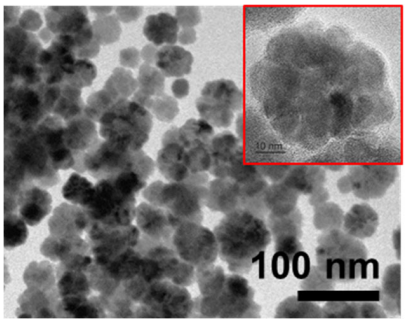
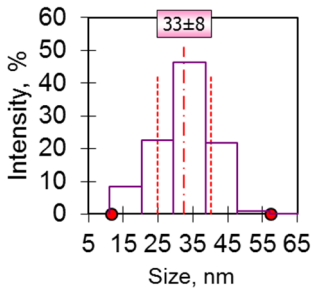
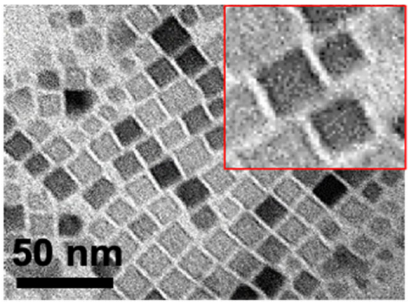
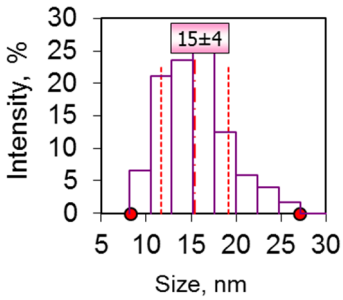
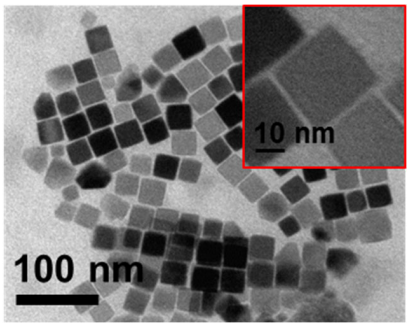
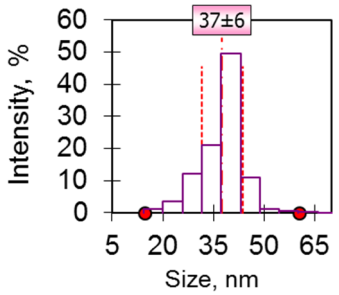
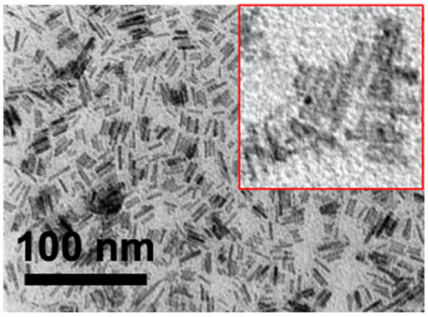
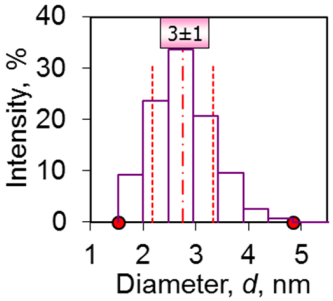
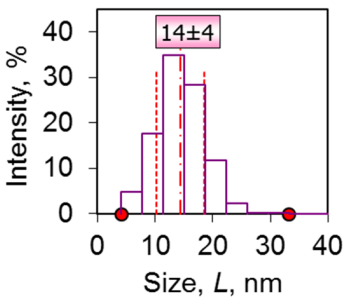
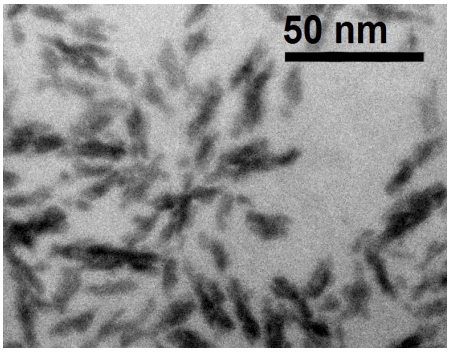
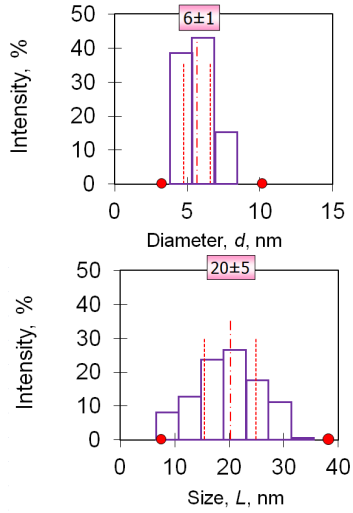
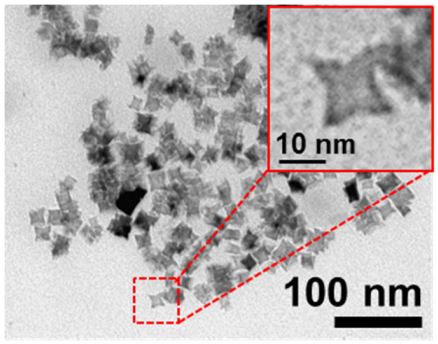
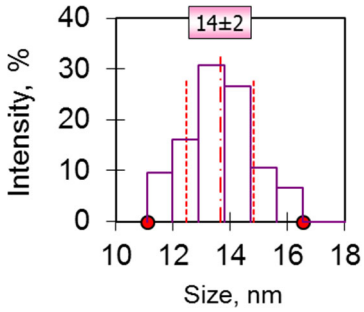
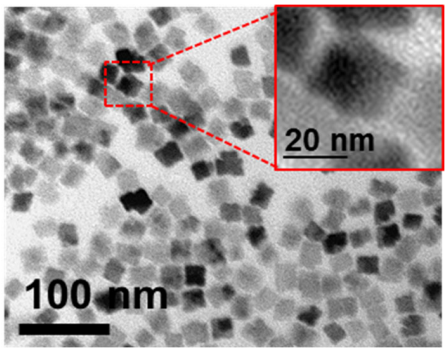
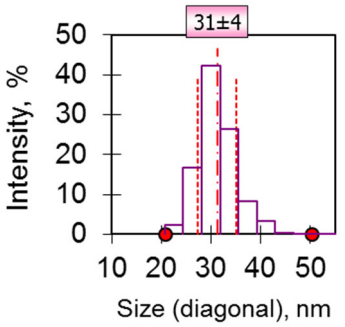
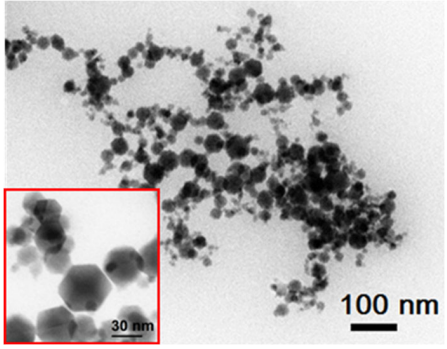
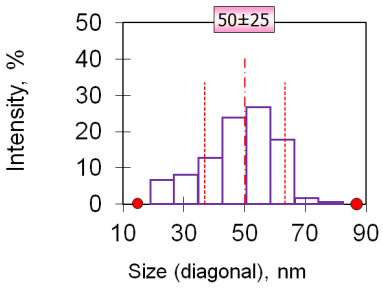
	Shape **Size of Magnetic Core [nm]** **Phase Composition**	**Microphotograph of NPs**	**Size Distribution**
2	Sphere-clusters 35 nm 35 ± 7 nm Fe_3O_4		
3	Cube 15 nm 15 ± 4 nm Fe_3O_4		
4	Cube 37 nm 37 ± 6 nm Fe_3O_4		
5	Rods 14 nm 14 ± 4 nm (length), 3 ± 1 nm (diameter) *β*-FeOOH		 

Table 2. *Cont.*

	Shape **Size of Magnetic Core [nm]** **Phase Composition**	**Microphotograph of NPs**	**Size Distribution**
6	Rods 20 nm 20 ± 5 nm (length) 6 ± 1 nm (diameter) iron carboxymaltose		
7	Octopodes 14 nm 14 ± 2 nm Fe_3O_4		
8	Octopodes 31 nm 31 ± 4 nm $CoFe_2O_4$		
9	Hexagons 50 nm 50 ± 25 nm γ-Fe_2O_3		

3.2. Measurements in RhB Solutions

The change in the fluorescence lifetime of RhB in aqueous solution was preliminarily measured in the operating range of the excitation laser radiation at 25 °C room temperature. The RhB solution at a concentration of 0.01 mg/mL had a sufficient fluorescence signal level and a monoexponential fluorescence decay profile. When the power density of the scanning laser radiation exceeded 0.48 MW/cm^2, a slight heating of the RhB solution began, as evidenced by the reduced fluorescence lifetime of RhB (Figure 2a). Therefore, excitation power densities less than 0.48 MW/cm^2 were used in experiments on cells with IONPs. The measured fluorescence lifetime of RhB aqueous solution as a function of the thermostat temperature in the range 20–60 °C, recorded at an excitation power density of 0.24 MW/cm^2, showed a linear relationship with (r^2 = 0.987) from 1.65 ± 0.06 ns at 20 °C to 1.39 ± 0.05 ns at 60 °C (Figure 2b).

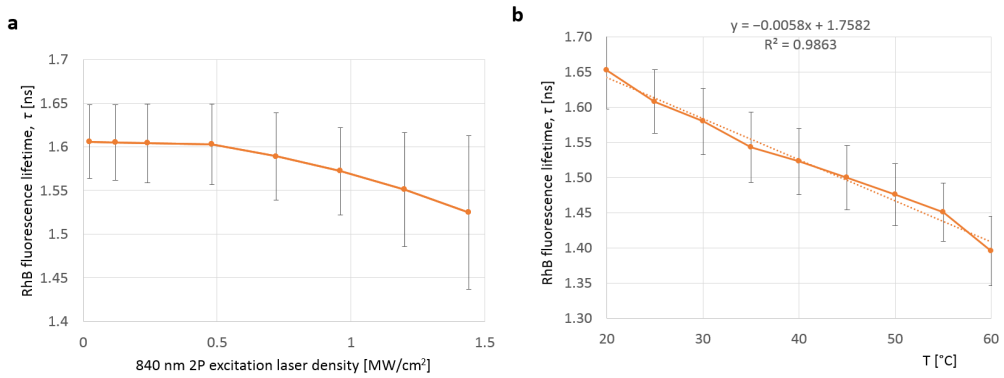
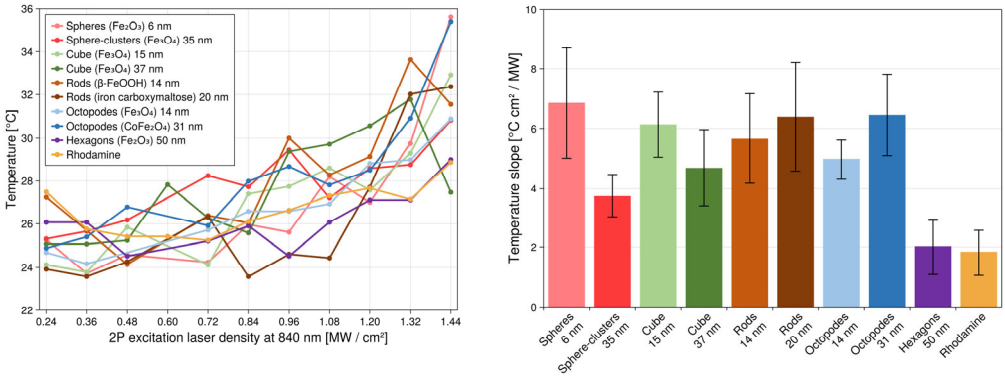


Figure 2. Fluorescence lifetime of RhB as a function of the power density of the 840-nm excitation laser (**a**) and temperature (**b**).

Aqueous colloids of 0.1 mg/L of IONPs with RhB at an initial temperature of 25 °C were scanned with an 840 nm laser at increasing power densities, and the fluorescence lifetime of RhB was recorded, from which the heating of the colloids was determined (Figure 3a). The relationship between temperature and power density was analyzed by linear regression, and the values of the slope and their standard errors were obtained (Figure 3b).



(**a**) (**b**)

Figure 3. Dependencies of the temperature determined by the RhB fluorescence lifetime during laser scanning (**a**) and slopes between temperature and laser power density ±SE (**b**).

Almost all colloids of the studied NPs showed insignificant heating of the surrounding aqueous medium by no more than 10 °C, as determined from the fluorescence lifetime of RhB when laser scanned at power densities up to 1.44 MW/cm^2.

3.3. Assessing the Temperature in Cells

First, the fluorescence lifetime of RhB accumulated in cells when heated by an incubator in a microscope slide in the temperature range of 20–60 °C was recorded. The characteristic lifetime of RhB bound to mitochondria was longer than in aqueous solution, ranging from 2.5 ± 0.1 ns (20 °C) to 2.2 ± 0.1 ns (60 °C). The longer fluorescence lifetime of RhB inside cells can be explained by its localization in mitochondrial membranes, which have a viscosity two orders of magnitude higher than water [51].

After accumulation of IONPs, cells were scanned with an 840 nm laser at a power density of 0.48 MW/cm^2 at room temperature and images of the fluorescence lifetime of RhB were recorded. Areas of cytoplasm were observed in the cell volume (when imaged in transmitted light, these areas contained vesicles) that exhibited a shortened RhB fluorescence lifetime (Figure 4). To analyze these areas, pixels with short lifetimes were extracted from the time-resolved image using a phasor diagram (Figure 4).

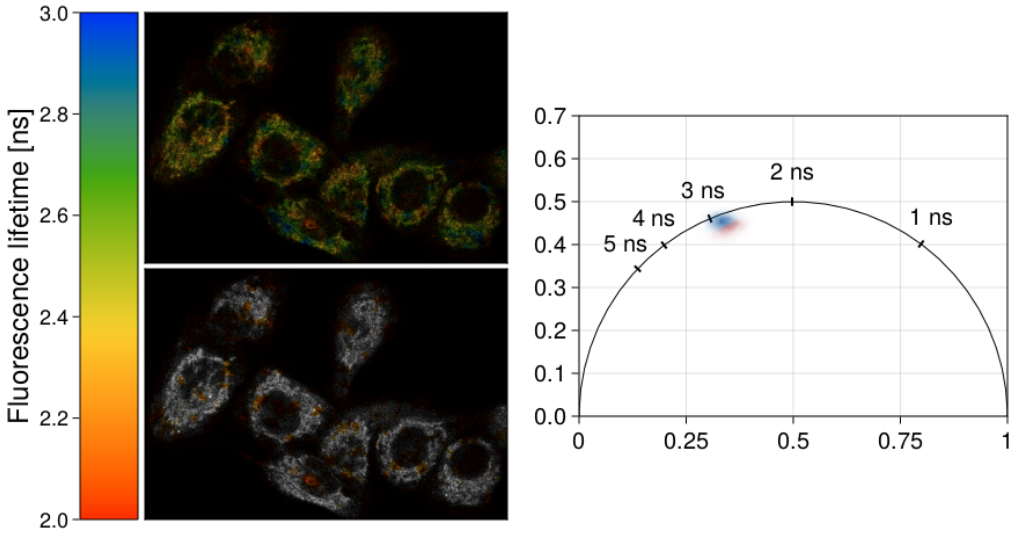


Figure 4. Fluorescence lifetime image of RhB in HeLa after accumulation of spherical cluster NPs under laser scanning at 0.48 MW/cm^2 power density (**top left**). Selection of "hot spots" in cells established by the fluorescence lifetime of RhB (**bottom left**, colored pixels). Phasor diagram of the fluorescence lifetime image with "hot spots" highlighted in red.

The results for the temperature assessment for IONPs in cells are shown in Figure 5.

When the temperature dependence of the fluorescence lifetime of RhB inside cells is approximated by a straight line, the estimated temperature for "hot spots" with IONPs exceeds 100 °C and reaches 120–150 °C. The temperature for "hot spots" also increases with the increase of NPs size: Fe_2O_3 spheres 6 nm—(122.574 ± 48.5) °C, Fe_3O_4 cube 15 nm—(129.295 ± 55.4) °C, Fe_3O_4 cube 37 nm—(133.777 ± 68.5) °C, Fe_3O_4 sphere-clusters 35 nm—(139.335 ± 59.4) °C, Fe_2O_3 hexagons 50 nm—(154.077 ± 47.0) °C. "Hot spots" for β-FeOOH 14 nm rods—(95.7655 ± 30.3) °C coincide with "hot spots" for Fe_3O_4 14 nm octopods—(95.6931 ± 41.3) °C. For slightly larger iron carboxymaltose rods, 20 nm, with $Fe(OH)_3$ nuclei, "hot spots" of (119.036 ± 46.0) °C coincide with "hot spots" of $CoFe_2O_4$ 31 nm octopods—(120.614 ± 48.6) °C. Such uncertainty in temperature values is due to the variation of fluorescence lifetimes in "hot spots".

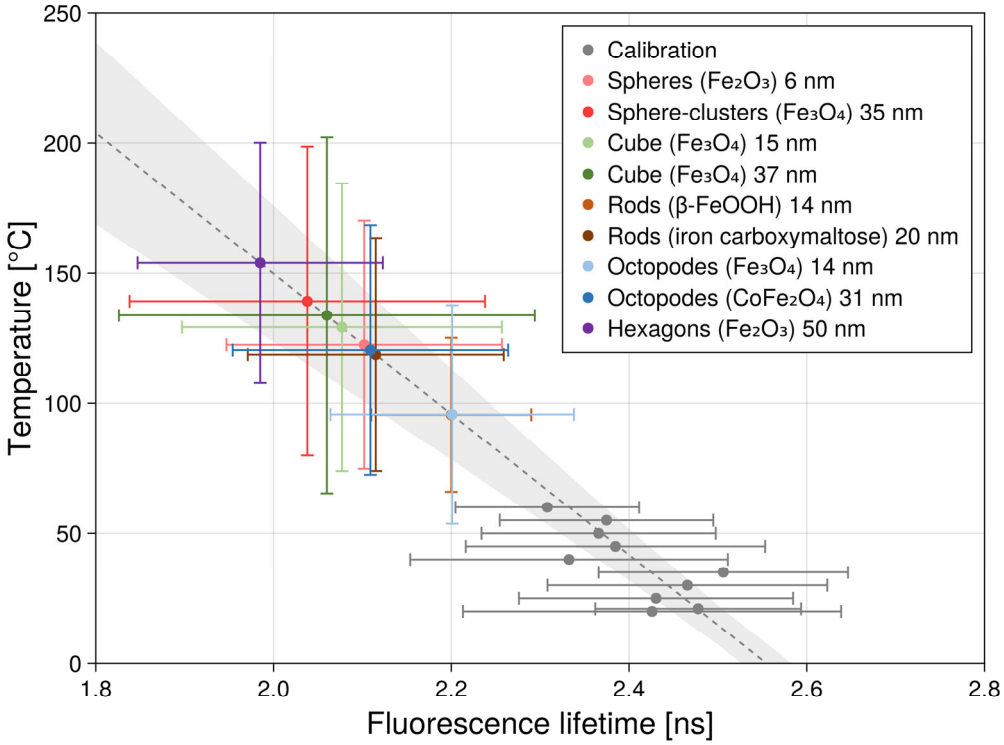


Figure 5. Distribution of RhB fluorescence lifetimes inside cells during thermostat heating (gray dots) and approximation by the temperature dependence for "hot spots" in cells with IONPs. The dotted line and the shaded area correspond to the temperature-lifetime relationship with a 95% confidence interval.

We did not find refractive indexes and extinction coefficients for β-FeOOH, $Fe(OH)_3$ and $CoFe_2O_4$ materials in the databases. However, there are separate publications with measurements that allow us to conclude that β-FeOOH is close to the Fe_3O_4 oxide in terms of optical properties [52], and the $CoFe_2O_4$ is greater to the Fe_2O_3 [53]. Here, in cellular experiments, we can only observe the most obvious patterns related to the temperature of the "hot spots", as we have not studied the uptake of synthesized NPs by TEM and we cannot reliably assess the number of NPs in the ensemble inside lysosomes.

3.4. Modelling

The extinction cross sections for the studied single Fe_3O_4 and Fe_2O_3 NPs of various shapes and sizes depending on the wavelength are shown in Figure 6.

It can be seen that with an increase in the NP size, the extinction cross section increases, while the extinction cross section is slightly larger for cubic NPs. The shape of the dependence for Fe_2O_3 oxide differs significantly from that of Fe_3O_4: for Fe_2O_3, a clearly defined maximum is observed at a wavelength of 420 nm, while the dependence for Fe_3O_4 does not have clearly defined maxima; more intense absorption is observed in the blue part of the spectrum.

The scattering, absorption, and extinction cross sections for ensembles of Fe_3O_4 NPs are shown in Figure 7.

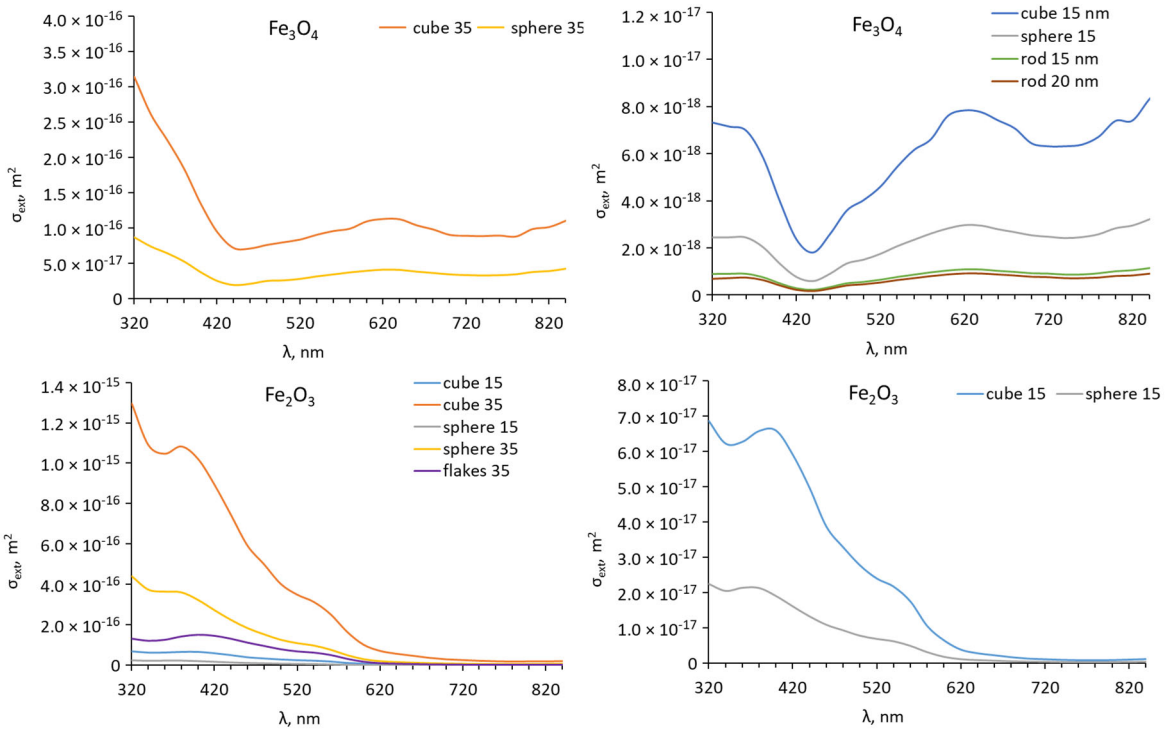


Figure 6. The extinction cross sections for the Fe_3O_4 and Fe_2O_3 NPs of various shapes and sizes depending on the wavelength. The graphs on the left show the curves for the NPs with the smallest extinction cross sections values.

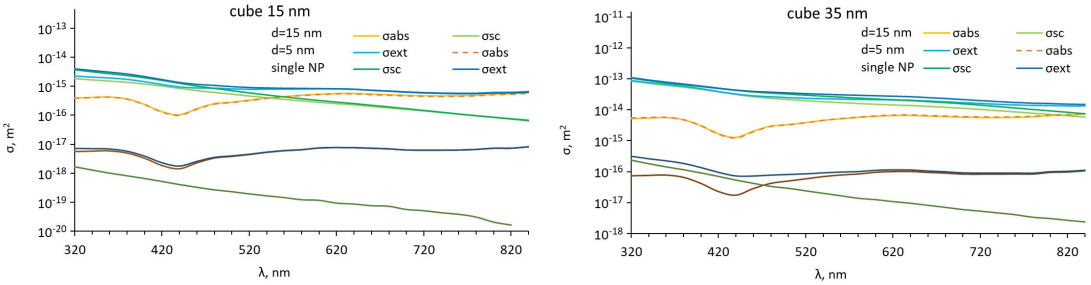


Figure 7. The extinction, absorption and scattering cross sections for the Fe_3O_4 NPs single NPs and arrays 5 × 5 × 3, distance between NPs d = 5 and 15 nm.

The shape of the dependence of the extinction cross section on the wavelength does not change for an ensemble of NPs. An increase in the number of particles in an ensemble also leads to a decrease in the distance between the particles, resulting in an increase in the absorption cross section.

Maps of the normalized electric field (E/E_0) distribution for Fe_3O_4 NPs of various shapes and sizes, as well as maps of the temperature distribution in the medium (irradiation time—1 μs) for 420 nm wavelength are shown in Figure 8.

Depending on the NP shape, a significant change in the spatial distribution of the field near the NP surface is observed. For cubic NPs, a high-intensity EM field is observed, localized in nanometer-sized regions near the cube vertices. The temperature field is uniformly distributed in the volume near the NPs. The obtained values for field enhancement and temperature are shown in Table 3.

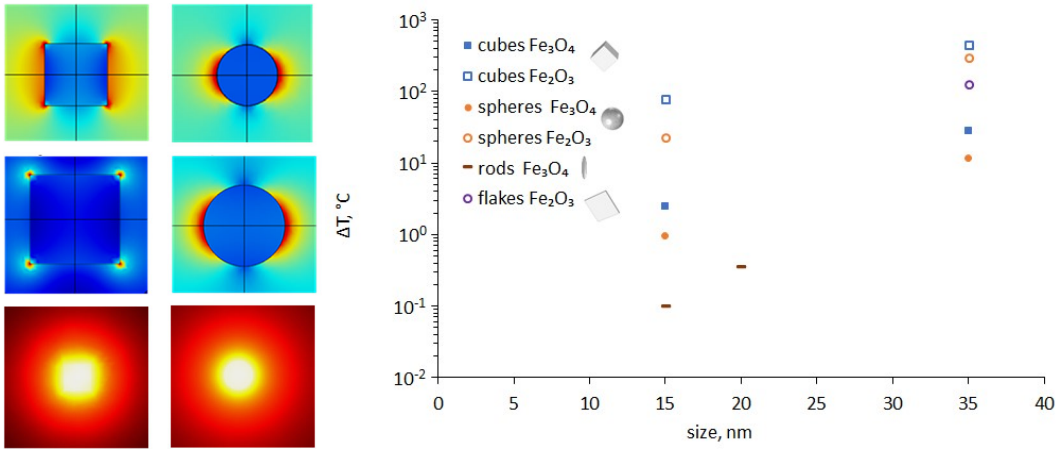


Figure 8. Maps of the normalized electric field (E/E_0) distribution and temperature for the studied Fe_3O_4 NPs as a function of size and shape: cubes and spheres of 15 and 35 nm size (**left**). Dependence of the heating temperature on the size, shape and material of the NPs for a wavelength of 420 nm (**right**).

Table 3. Local field enhancement and temperature increase relative to surrounding medium for studied IONPs for 420 and 840 nm wavelengths.

NPs		ΔT, °C	$\lvert E/E_0 \rvert$	ΔT, °C	$\lvert E/E_0 \rvert$
		λ = 420 nm		λ = 840 nm	
		Fe_3O_4			
cubes 15 nm	single NP	2.5	1.4	5.6	1.2
	array 3 × 3 × 3	55.9	1.5	127.0	1.3
	array 5 × 5 × 3	154.0	1.7	355.0	1.5
cubes 35 nm	single NP	28.8	1.8	66.7	1.2
spheres 15 nm	single NP	1.0	2.2	2.3	1.8
spheres 35 nm	single NP	11.8	2.0	26.7	1.8
rods 15 nm	single NP (along x)	0.0	1.6	0.1	1.5
	single NP (along y)	0.1	2.3	0.2	1.5
	single NP (along z)	0.0	1.6	0.1	2.2
rods 20 nm	single NPs (along x)	0.1	1.6	0.3	1.5
	single NP (along y)	0.4	2.5	0.8	1.7
	single NP (along z)	0.1	1.6	0.3	1.6
		Fe_2O_3			
cubes 15 nm	single NP	76.8	1.6	0.8	1.4
cubes 35 nm	single NP	450.0	3.1	9.5	1.7
spheres 15 nm	single NP	22.6	2.9	0.3	2.1
spheres 35 nm	single NP	292.0	2.6	3.3	2.1
flakes 35 nm	single NP	124.0	2.3	1.2	1.7

It can be seen that the heating temperature increases with increasing nanoparticle size, while the heating is higher for cubic NPs, which is probably due to a large field enhancement due to higher localization. The higher heating temperature of the Fe_2O_3 NPs is due to the higher absorption cross section at the 420 nm wavelength. At the same time,

practically no heating is observed for Fe_2O_3 NPs at a wavelength of 840 nm, where the absorption cross section is significantly lower than for Fe_3O_4.

However, the heating temperatures obtained for single IONPs are lower than those measured experimentally in cells. We assumed that the higher temperature measured experimentally may be due to the local accumulation of NPs in lysosomes, resulting in a large number of NPs in close proximity. To test this hypothesis, heating simulations were performed for the ensembles. The dependence of the heating temperature on the ensemble size for 15 nm cubic NPs is shown in Figure 9.

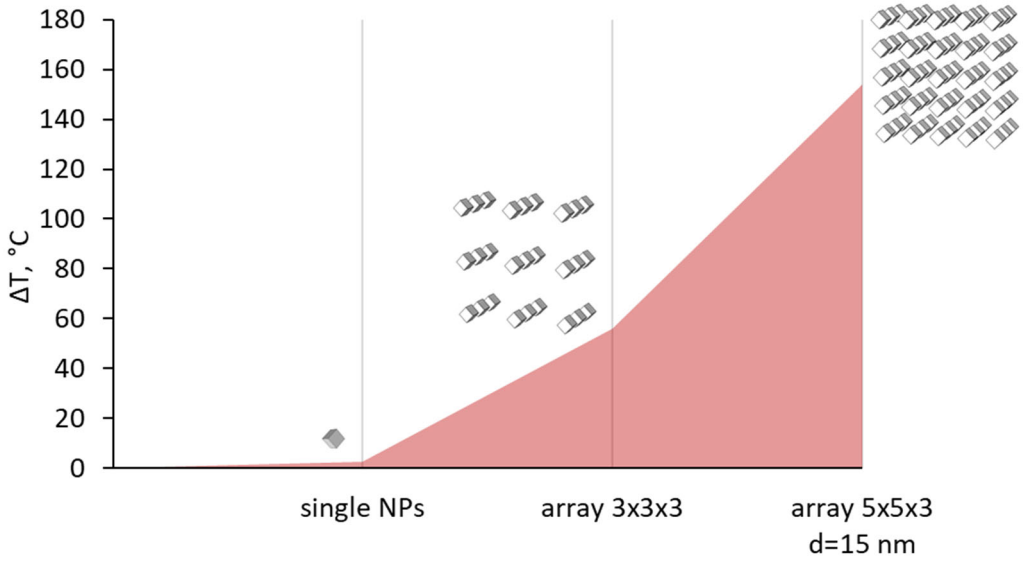


Figure 9. Dependence of the heating temperature on the ensemble size for 15 nm cubic NPs.

It has been shown that the local heating of NPs in an ensemble reaches sufficiently high values, the relative temperature change is about 154 °C for Fe_3O_4 5 × 5 × 3 NPs array d = 15 nm.

To interpret the experiment on estimating the heating temperature of the studied NPs in water, we simulated the heating of an ensemble of Fe_3O_4 NPs 5 × 5 × 3 in size in water. Distribution maps of the relative temperature change (difference between the NP heating temperature and room temperature) for the studied ensembles in a cage and in water are shown in the Figure 10.

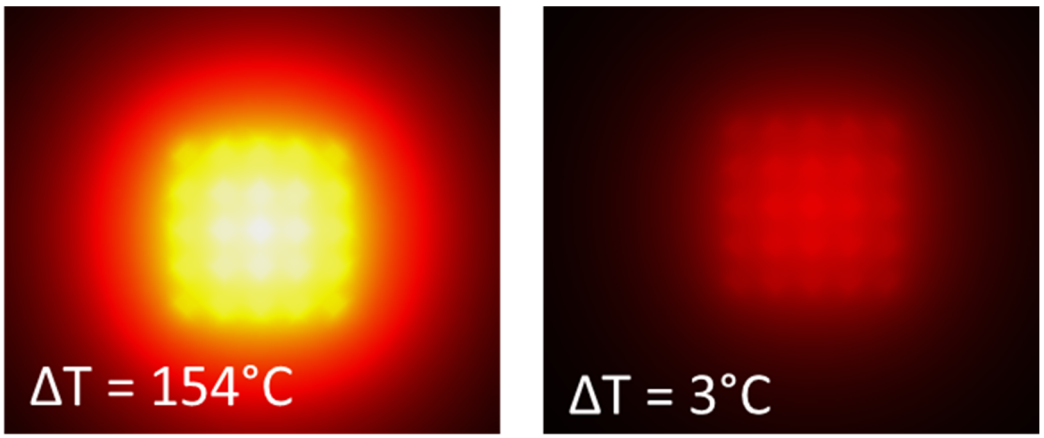


Figure 10. Distribution maps of the relative temperature change during heating of ensembles of iron oxide NPs Fe_3O_4 array 5 × 5 × 3 d = 15 nm in cells and in water.

We assume that when NPs are placed in a medium with a higher thermal conductivity, an effective heat exchange with the medium occurs, resulting in heat dissipation occurs, and the heating temperature of the ensemble does not reach high values.

4. Discussion

Photothermal therapy is based on raising the temperature of the tumor cells above 42 °C. This is done by illuminating the cells must be illuminated with a laser and converting the radiation energy into heat. Certain types of NPs, called photothermal agents, can convert light into heat. The temperature increase in the tumor depends on the efficiency of the photothermal conversion, the concentration of photothermal agents in the tumor, and the dose of the light applied [54]. Since reliable biosafety in the human body is a basic requirement for any cancer treatment, IONPs appear to be promising photothermal agents [55]. They have several advantages, such as excellent magnetic properties, good compatibility and no toxicity [56]. The magnetic properties of IONPs allow their use as contrast agents in MRI. The main disadvantage of IONPs is the high radiation dose required for complete tumor ablation. One approach to solve this problem is through clustering of IONPs, which demonstrated a significant increase in laser radiation absorption and heating compared to non-aggregated IONPs [18,57,58]. On the other hand, the heating efficiency can be increased by magnetic hyperthermia, which gives the ions the dual ability to act as magnetic and photothermal agents.

A large number of studies are devoted to modeling the field enhancement near the surface of noble metal NPs [59,60]. Efforts are aimed at optimizing the size and shape of the NPs in order to obtain resonance in the near-infrared (NIR) region [61,62]. The Fe_3O_4 NPs studied in this work have resonance in the NIR region of 820–840 nm, which is promising for bioapplications. For ensembles of metal NPs, even a small change in the position of the NPs leads to a significant shift in the position of the plasmon resonance maximum and, consequently, the heating temperature [63]. The degree of localization and field enhancement near the surface of dielectric NPs is lower [7], but the resonance is observed in a wider wavelength range, so that they are not as sensitive to excitation, which is important for the reproducibility of experimental results on biological objects, such as cells, in which NPs are randomly distributed.

Infrared macro-scale thermal images actively demonstrate the heating of IONPs after laser irradiation in water, in cells, and in vivo [13]. There is no direct method for measuring the heating of IONPs. There are several works on indirect measurement of the local heating temperature of IONPs. For example, for a mixture of colloids of IONPs of different sizes, it has been demonstrated that it is possible to create several types of hot spots simultaneously, by selectively activating each population of IONPs by varying the magnetic field parameters. Thus, the local temperature increase measured using fluorescent proteins as a molecular thermometers on the surface of IONPs reached 85 °C [64]. The local thermometry results were in good agreement with the magnetic properties of each IONP and decreased slightly in the case of a thick polymer coating of the IONP, which creates a spacer between the surface of the IONPs and the molecular thermometer. An additional difficulty in the use of fluorescence thermometers is that the fluorescence signal intensity decreases with increasing temperature, which complicates the evaluation.

5. Conclusions

As a summary of modeling, we can say about four regularities for heating IONPs with light: (1) large NPs heat up better than small ones; (2) NPs ensembles are heated better than single NPs; (3) Fe_2O_3 is better than Fe_3O_4; (4) efficiency grows in a row of rods/flakes/spheres/cubes. However, the results with water IONPs colloids did not confirm such regularities. On the contrary, large spherical and cubic NPs heated up worse than small ones, and about the same as rod-like NPs. This distribution is probably due to different properties of the hydrophilic shells of NPs in relation to accessibility for RhB, -carboxymaltose and PEI for nanorods, DOPAC for cubic and spherical NPs.

In the experiment on cells, RhB bound to the mitochondrial membrane, and the IONPs uptaked in lysosomes; therefore, the thermometer and the IONPs ensemble were separated in space, and the NPs surface should not have affected the RhB fluorescence lifetime. In the experiment on cells, IONPs were heated more efficiently in the series: hexagonal (modeled with a flakes), spherical, cubic, rod-like, octopod-likes (modeled with a cubes). The regularities are also observed that large NPs of the same shape heat better than small ones and Fe_2O_3 is better than Fe_3O_4. Possibly, the incomplete compliance with the regularities derived from the modeling was due to a different cellular uptake of NPs, which we did not study in this work.

It has been demonstrated that the local heating of NPs in an ensemble can reach sufficiently high values for cell damage. When IONPs are placed in a medium with a higher thermal conductivity (for example, water), an effective heat exchange with the medium occurs, resulting in heat dissipation, and the heating temperature of the ensemble does not reach high values. The situation is different when IONPs are trapped inside the cell in lysosomes—lipid sacs with lower thermal conductivity. As a result, so-called "hot spots" with temperature above 100 °C can appear inside cells around the accumulation of IONPs in vesicles. The distribution of "hot spots" determines the thermal response of the entire biosample. It should have a certain effect on the cell death mechanism by hyperthermia and the reaction of lysosome destruction.

Supplementary Materials: The following supporting information can be downloaded at: https://www.mdpi.com/article/10.3390/photonics10070705/s1, Figure S1: XRD patterns of dry powders of synthesized NPs; Figure S2: ^{57}Fe Mössbauer spectrum at room temperature (293 K) of synthesized NPs.

Author Contributions: Conceptualization, A.R., I.R., D.P., R.S. and V.L.; methodology, A.R., A.N., P.O., E.P., N.M., I.R. and M.A.; synthesis, A.S., P.L., A.N., P.O. and M.A.; modelling, D.P. and I.R.; validation, K.L., A.R., I.R. and D.P.; formal analysis, D.P. and I.R.; investigation, A.R., D.P., I.M., A.S., P.L., A.N., P.O., E.P., N.M. and I.R.; resources, A.R., M.A., K.L., A.P. and V.L.; software data processing, I.R.; writing—original draft preparation, A.R. and D.P.; writing—review and editing, A.R., I.R. and D.P.; visualization, A.R, D.P. and I.R.; project administration and funding acquisition, A.R. All authors have read and agreed to the published version of the manuscript.

Funding: This research was funded by RFBR, grant No. 21-52-12030 NNIO_a and by the MES of the RF, grant for the creation and development of world-class research centers No. 075-15-2022-315 "Photonics".

Institutional Review Board Statement: Not applicable.

Informed Consent Statement: Not applicable.

Data Availability Statement: The data presented in this study are available on request from the corresponding author.

Acknowledgments: The authors are grateful to Center for collective use No. 74834 "Technological and diagnostic center for the production, research and certification of micro and nanostructures" in GPI RAS.

Conflicts of Interest: The authors declare no conflict of interest. The funders had no role in the design of the study; in the collection, analyses, or interpretation of data; in the writing of the manuscript; or in the decision to publish the results.

References

1. Sharma, S.K.; Shrivastava, N.; Rossi, F.; Tung, L.D.; Thanh, N.T.K. Nanoparticles-Based Magnetic and Photo Induced Hyperthermia for Cancer Treatment. *Nano Today* **2019**, *29*, 100795. [CrossRef]
2. Sun, R.; Chen, H.; Sutrisno, L.; Kawazoe, N.; Chen, G. Nanomaterials and Their Composite Scaffolds for Photothermal Therapy and Tissue Engineering Applications. *Sci. Technol. Adv. Mater.* **2021**, *22*, 404–428. [CrossRef] [PubMed]
3. Liu, Z.; Boltasseva, A.; Pedersen, R.H.; Bakker, R.; Kildishev, A.V.; Drachev, V.P.; Shalaev, V.M. Plasmonic Nanoantenna Arrays for the Visible. *Metamaterials* **2008**, *2*, 45–51. [CrossRef]

4. Hatab, N.A.; Hsueh, C.-H.; Gaddis, A.L.; Retterer, S.T.; Li, J.-H.; Eres, G.; Zhang, Z.; Gu, B. Free-Standing Optical Gold Bowtie Nanoantenna with Variable Gap Size for Enhanced Raman Spectroscopy. *Nano Lett.* **2010**, *10*, 4952–4955. [CrossRef]
5. Nien, L.-W.; Lin, S.-C.; Chao, B.-K.; Chen, M.-J.; Li, J.-H.; Hsueh, C.-H. Giant Electric Field Enhancement and Localized Surface Plasmon Resonance by Optimizing Contour Bowtie Nanoantennas. *J. Phys. Chem. C* **2013**, *117*, 25004–25011. [CrossRef]
6. Giannini, V.; Fernández-Domínguez, A.I.; Heck, S.C.; Maier, S.A. Plasmonic Nanoantennas: Fundamentals and Their Use in Controlling the Radiative Properties of Nanoemitters. *Chem. Rev.* **2011**, *111*, 3888–3912. [CrossRef]
7. Baranov, D.G.; Zuev, D.A.; Lepeshov, S.I.; Kotov, O.V.; Krasnok, A.E.; Evlyukhin, A.B.; Chichkov, B.N. All-Dielectric Nanophotonics: The Quest for Better Materials and Fabrication Techniques. *Optica* **2017**, *4*, 814. [CrossRef]
8. Shi, L.; Fenollosa, R.; Tuzer, T.U.; Meseguer, F. Angle-Dependent Quality Factor of Mie Resonances in Silicon-Colloid-Based Microcavities. *ACS Photonics* **2014**, *1*, 408–412. [CrossRef]
9. Ma, C.; Yan, J.; Wei, Y.; Liu, P.; Yang, G. Enhanced Second Harmonic Generation in Individual Barium Titanate Nanoparticles Driven by Mie Resonances. *J. Mater. Chem. C* **2017**, *5*, 4810–4819. [CrossRef]
10. Lozano-Pedraza, C.; Plaza-Mayoral, E.; Espinosa, A.; Sot, B.; Serrano, A.; Salas, G.; Blanco-Andujar, C.; Cotin, G.; Felder-Flesch, D.; Begin-Colin, S.; et al. Assessing the Parameters Modulating Optical Losses of Iron Oxide Nanoparticles under near Infrared Irradiation. *Nanoscale Adv.* **2021**, *3*, 6490–6502. [CrossRef]
11. Boltasseva, A.; Atwater, H.A. Low-Loss Plasmonic Metamaterials. *Science* **2011**, *331*, 290–291. [CrossRef]
12. Vallejo-Fernandez, G.; Whear, O.; Roca, A.G.; Hussain, S.; Timmis, J.; Patel, V.; O'Grady, K. Mechanisms of Hyperthermia in Magnetic Nanoparticles. *J. Phys. D Appl. Phys.* **2013**, *46*, 312001. [CrossRef]
13. Espinosa, A.; Kolosnjaj-Tabi, J.; Abou-Hassan, A.; Sangnier, A.P.; Curcio, A.; Silva, A.K.A.; Di Corato, R.; Neveu, S.; Pellegrino, T.; Liz-Marzán, L.M.; et al. Magnetic (Hyper) Thermia or Photothermia? Progressive Comparison of Iron Oxide and Gold Nanoparticles Heating in Water, in Cells, and In Vivo. *Adv. Funct. Mater.* **2018**, *28*, 1803660. [CrossRef]
14. Zhao, S.; Yu, X.; Qian, Y.; Chen, W.; Shen, J. Multifunctional Magnetic Iron Oxide Nanoparticles: An Advanced Platform for Cancer Theranostics. *Theranostics* **2020**, *10*, 6278–6309. [CrossRef]
15. Espinosa, A.; Di Corato, R.; Kolosnjaj-Tabi, J.; Flaud, P.; Pellegrino, T.; Wilhelm, C. Duality of Iron Oxide Nanoparticles in Cancer Therapy: Amplification of Heating Efficiency by Magnetic Hyperthermia and Photothermal Bimodal Treatment. *ACS Nano* **2016**, *10*, 2436–2446. [CrossRef]
16. Yan, H.; Shang, W.; Sun, X.; Zhao, L.; Wang, J.; Xiong, Z.; Yuan, J.; Zhang, R.; Huang, Q.; Wang, K.; et al. "All-in-One" Nanoparticles for Trimodality Imaging-Guided Intracellular Photo-magnetic Hyperthermia Therapy under Intravenous Administration. *Adv. Funct. Mater.* **2018**, *28*, 1705710. [CrossRef]
17. Lin, S.-Y.; Huang, R.-Y.; Liao, W.-C.; Chuang, C.-C.; Chang, C.-W. Multifunctional PEGylated Albumin/IR780/Iron Oxide Nanocomplexes for Cancer Photothermal Therapy and MR Imaging. *Nanotheranostics* **2018**, *2*, 106–116. [CrossRef]
18. Cabana, S.; Curcio, A.; Michel, A.; Wilhelm, C.; Abou-Hassan, A. Iron Oxide Mediated Photothermal Therapy in the Second Biological Window: A Comparative Study between Magnetite/Maghemite Nanospheres and Nanoflowers. *Nanomaterials* **2020**, *10*, 1548. [CrossRef]
19. Liang, X.; Chen, M.; Bhattarai, P.; Hameed, S.; Tang, Y.; Dai, Z. Complementing Cancer Photodynamic Therapy with Ferroptosis through Iron Oxide Loaded Porphyrin-Grafted Lipid Nanoparticles. *ACS Nano* **2021**, *15*, 20164–20180. [CrossRef] [PubMed]
20. Penon, O.; Marín, M.J.; Amabilino, D.B.; Russell, D.A.; Pérez-García, L. Iron Oxide Nanoparticles Functionalized with Novel Hydrophobic and Hydrophilic Porphyrins as Potential Agents for Photodynamic Therapy. *J. Colloid Interface Sci.* **2016**, *462*, 154–165. [CrossRef] [PubMed]
21. Pominova, D.V.; Romanishkin, I.D.; Plotnikova, E.A.; Morozova, N.B.; Loschenov, V.B.; Wittig, R.; Linden, M.; Steiner, R.W.; Ryabova, A.V. Photo-Induced Processes of Iron Oxide Nanoparticles to Enhance Laser Therapy. *Biomed. Photonics* **2022**, *10*, 44–58. [CrossRef]
22. Zhou, J.; del Rosal, B.; Jaque, D.; Uchiyama, S.; Jin, D. Advances and Challenges for Fluorescence Nanothermometry. *Nat. Methods* **2020**, *17*, 967–980. [CrossRef]
23. Mercadé-Prieto, R.; Rodriguez-Rivera, L.; Chen, X.D. Fluorescence Lifetime of Rhodamine B in Aqueous Solutions of Polysaccharides and Proteins as a Function of Viscosity and Temperature. *Photochem. Photobiol. Sci.* **2017**, *16*, 1727–1734. [CrossRef]
24. von Steyern, F.V.; Josefsson, J.O.; Tågerud, S. Rhodamine B, a Fluorescent Probe for Acidic Organelles in Denervated Skeletal Muscle. *J. Histochem. Cytochem.* **1996**, *44*, 267–274. [CrossRef] [PubMed]
25. Reungpatthanaphong, P.; Dechsupa, S.; Meesungnoen, J.; Loetchutinat, C.; Mankhetkorn, S. Rhodamine B as a Mitochondrial Probe for Measurement and Monitoring of Mitochondrial Membrane Potential in Drug-Sensitive and -Resistant Cells. *J. Biochem. Biophys. Methods* **2003**, *57*, 1–16. [CrossRef] [PubMed]
26. Moreau, D.; Lefort, C.; Burke, R.; Leveque, P.; O'Connor, R.P. Rhodamine B as an Optical Thermometer in Cells Focally Exposed to Infrared Laser Light or Nanosecond Pulsed Electric Fields. *Biomed. Opt. Express* **2015**, *6*, 4105. [CrossRef]
27. Fan, X.; Teng, C.P.; Yeo, J.C.C.; Li, Z.; Wang, T.; Chen, H.; Jiang, L.; Hou, X.; He, C.; Liu, J. Temperature and PH Responsive Light-Harvesting System Based on AIE-Active Microgel for Cell Imaging. *Macromol. Rapid Commun.* **2021**, *42*, 2000716. [CrossRef]
28. Kumar, A.; Goudar, V.S.; Kaladharan, K.; Santra, T.S.; Tseng, F.-G. Synthesis and Characterization of a Fluorescent Polymeric Nano-Thermometer: Dynamic Monitoring of 3D Temperature Distribution in Co-Cultured Tumor Spheroids. *Analyst* **2023**, *148*, 2045–2057. [CrossRef] [PubMed]

29. Arai, S.; Suzuki, M.; Park, S.-J.; Yoo, J.S.; Wang, L.; Kang, N.-Y.; Ha, H.-H.; Chang, Y.-T. Mitochondria-Targeted Fluorescent Thermometer Monitors Intracellular Temperature Gradient. *Chem. Commun.* **2015**, *51*, 8044–8047. [CrossRef]
30. 1309-37-1-Iron(III) Oxide, Industrial, NanoArc®-45007-Alfa Aesar. Available online: https://www.alfa.com/ru/catalog/045007/ (accessed on 5 May 2023).
31. Vifor Pharma. Iron Products. Available online: https://www.viforpharma.com/products/iron-products (accessed on 5 May 2023).
32. Ostroverkhov, P.V.; Semkina, A.S.; Naumenko, V.A.; Plotnikova, E.A.; Melnikov, P.A.; Abakumova, T.O.; Yakubovskaya, R.I.; Mironov, A.F.; Vodopyanov, S.S.; Abakumov, A.M.; et al. Synthesis and Characterization of Bacteriochlorin Loaded Magnetic Nanoparticles (MNP) for Personalized MRI Guided Photosensitizers Delivery to Tumor. *J. Colloid Interface Sci.* **2019**, *537*, 132–141. [CrossRef]
33. Naumenko, V.; Nikitin, A.; Kapitanova, K.; Melnikov, P.; Vodopyanov, S.; Garanina, A.; Valikhov, M.; Ilyasov, A.; Vishnevskiy, D.; Markov, A.; et al. Intravital Microscopy Reveals a Novel Mechanism of Nanoparticles Excretion in Kidney. *J. Control. Release* **2019**, *307*, 368–378. [CrossRef] [PubMed]
34. Nikitin, A.A.; Yurenya, A.Y.; Zatsepin, T.S.; Aparin, I.O.; Chekhonin, V.P.; Majouga, A.G.; Farle, M.; Wiedwald, U.; Abakumov, M.A. Magnetic Nanoparticles as a Tool for Remote DNA Manipulations at a Single-Molecule Level. *ACS Appl. Mater. Interfaces* **2021**, *13*, 14458–14469. [CrossRef]
35. Nikitin, A.; Khramtsov, M.; Garanina, A.; Mogilnikov, P.; Sviridenkova, N.; Shchetinin, I.; Savchenko, A.; Abakumov, M.; Majouga, A. Synthesis of Iron Oxide Nanorods for Enhanced Magnetic Hyperthermia. *J. Magn. Magn. Mater.* **2019**, *469*, 443–449. [CrossRef]
36. Shelekhov, E.V.; Sviridova, T.A. Programs for X-ray Analysis of Polycrystals. *Met. Sci. Heat Treat.* **2000**, *42*, 309–313. [CrossRef]
37. Farooq, S.; de Araujo, R.E. Engineering a Localized Surface Plasmon Resonance Platform for Molecular Biosensing. *Open J. Appl. Sci.* **2018**, *08*, 126–139. [CrossRef]
38. Kholodtsova, M.N.; Grachev, P.V.; Blondel, W.C.; Zelenkov, P.V.; Potapov, A.A.; Shcherbakov, I.A.; Loschenov, V.B. Application of Devices for Space-Resolved Spectroscopy on the Example of Two-Layer Phantoms Containing Metallic Nanoparticles. *BMP* **2018**, *7*, 4–12. [CrossRef]
39. Rakić, A.D.; Djurišić, A.B.; Elazar, J.M.; Majewski, M.L. Optical Properties of Metallic Films for Vertical-Cavity Optoelectronic Devices. *Appl. Opt.* **1998**, *37*, 5271. [CrossRef]
40. Querry, M.R. *Optical Constants*; Technical Reports and Bulletins; Defense Technical Information Center: Kansas City, MO, USA, 1985.
41. Rashidi, S.; Karimi, N.; Mahian, O.; Abolfazli Esfahani, J. A Concise Review on the Role of Nanoparticles upon the Productivity of Solar Desalination Systems. *J. Therm. Anal. Calorim.* **2019**, *135*, 1145–1159. [CrossRef]
42. Iron Oxide, Hematite (Fe_2O_3). Available online: https://janaf.nist.gov/tables/Fe-030.html (accessed on 5 May 2023).
43. *NIST-JANAF Thermochemical Tables*, 4th ed.; Chase, M.W.; National Institute of Standards and Technology (USA) (Eds.) American Chemical Society; American Institute of Physics for the National Institute of Standards and Technology: Washington, DC, USA, 1998; ISBN 978-1-56396-831-0.
44. Lu, K.; Wazawa, T.; Sakamoto, J.; Vu, C.Q.; Nakano, M.; Kamei, Y.; Nagai, T. Intracellular Heat Transfer and Thermal Property Revealed by Kilohertz Temperature Imaging with a Genetically Encoded Nanothermometer. *Nano Lett.* **2022**, *22*, 5698–5707. [CrossRef]
45. Song, P.; Gao, H.; Gao, Z.; Liu, J.; Zhang, R.; Kang, B.; Xu, J.-J.; Chen, H.-Y. Heat Transfer and Thermoregulation within Single Cells Revealed by Transient Plasmonic Imaging. *Chem* **2021**, *7*, 1569–1587. [CrossRef]
46. Hoejholt, K.L.; Mužić, T.; Jensen, S.D.; Dalgaard, L.T.; Bilgin, M.; Nylandsted, J.; Heimburg, T.; Frandsen, S.K.; Gehl, J. Calcium Electroporation and Electrochemotherapy for Cancer Treatment: Importance of Cell Membrane Composition Investigated by Lipidomics, Calorimetry and in Vitro Efficacy. *Sci. Rep.* **2019**, *9*, 4758. [CrossRef] [PubMed]
47. Baffou, G.; Quidant, R.; Girard, C. Heat Generation in Plasmonic Nanostructures: Influence of Morphology. *Appl. Phys. Lett.* **2009**, *94*, 153109. [CrossRef]
48. Gervits, N.E.; Gippius, A.A.; Tkachev, A.V.; Demikhov, E.I.; Starchikov, S.S.; Lyubutin, I.S.; Vasiliev, A.L.; Chekhonin, V.P.; Abakumov, M.A.; Semkina, A.S.; et al. Magnetic Properties of Biofunctionalized Iron Oxide Nanoparticles as Magnetic Resonance Imaging Contrast Agents. *Beilstein J. Nanotechnol.* **2019**, *10*, 1964–1972. [CrossRef]
49. Nikitin, A.A.; Shchetinin, I.V.; Tabachkova, N.Y.; Soldatov, M.A.; Soldatov, A.V.; Sviridenkova, N.V.; Beloglazkina, E.K.; Savchenko, A.G.; Fedorova, N.D.; Abakumov, M.A.; et al. Synthesis of Iron Oxide Nanoclusters by Thermal Decomposition. *Langmuir* **2018**, *34*, 4640–4650. [CrossRef]
50. Azevedo, R.C.S.; Sousa, R.G.; Macedo, W.A.A.; Sousa, E.M.B. Combining Mesoporous Silica–Magnetite and Thermally-Sensitive Polymers for Applications in Hyperthermia. *J. Sol-Gel Sci. Technol.* **2014**, *72*, 208–218. [CrossRef]
51. Steinmark, I.E.; James, A.L.; Chung, P.-H.; Morton, P.E.; Parsons, M.; Dreiss, C.A.; Lorenz, C.D.; Yahioglu, G.; Suhling, K. Targeted Fluorescence Lifetime Probes Reveal Responsive Organelle Viscosity and Membrane Fluidity. *PLoS ONE* **2019**, *14*, e0211165. [CrossRef]
52. Maeda, H.; Maeda, Y. Spectroscopic Ellipsometry Study on Refractive Index Spectra of Colloidal β-FeOOH Nanorods with Their Self-Assembled Thin Films. *Langmuir* **2011**, *27*, 2895–2903. [CrossRef]

53. Erdem, D.; Bingham, N.S.; Heiligtag, F.J.; Pilet, N.; Warnicke, P.; Heyderman, L.J.; Niederberger, M. $CoFe_2O_4$ and $CoFe_2O_4$-SiO_2 Nanoparticle Thin Films with Perpendicular Magnetic Anisotropy for Magnetic and Magneto-Optical Applications. *Adv. Funct. Mater.* **2016**, *26*, 1954–1963. [CrossRef]
54. Melamed, J.R.; Edelstein, R.S.; Day, E.S. Elucidating the Fundamental Mechanisms of Cell Death Triggered by Photothermal Therapy. *ACS Nano* **2015**, *9*, 6–11. [CrossRef]
55. Estelrich, J.; Busquets, M. Iron Oxide Nanoparticles in Photothermal Therapy. *Molecules* **2018**, *23*, 1567. [CrossRef]
56. Shi, D.; Sadat, M.E.; Dunn, A.W.; Mast, D.B. Photo-Fluorescent and Magnetic Properties of Iron Oxide Nanoparticles for Biomedical Applications. *Nanoscale* **2015**, *7*, 8209–8232. [CrossRef]
57. Shen, S.; Wang, S.; Zheng, R.; Zhu, X.; Jiang, X.; Fu, D.; Yang, W. Magnetic Nanoparticle Clusters for Photothermal Therapy with Near-Infrared Irradiation. *Biomaterials* **2015**, *39*, 67–74. [CrossRef] [PubMed]
58. Nemec, S.; Kralj, S.; Wilhelm, C.; Abou-Hassan, A.; Rols, M.-P.; Kolosnjaj-Tabi, J. Comparison of Iron Oxide Nanoparticles in Photothermia and Magnetic Hyperthermia: Effects of Clustering and Silica Encapsulation on Nanoparticles' Heating Yield. *Appl. Sci.* **2020**, *10*, 7322. [CrossRef]
59. Chung, T.; Lee, S.-Y.; Song, E.Y.; Chun, H.; Lee, B. Plasmonic Nanostructures for Nano-Scale Bio-Sensing. *Sensors* **2011**, *11*, 10907–10929. [CrossRef]
60. Montaño-Priede, J.L.; Pal, U. Estimating Near Electric Field of Polyhedral Gold Nanoparticles for Plasmon-Enhanced Spectroscopies. *J. Phys. Chem. C* **2019**, *123*, 11833–11839. [CrossRef]
61. Paria, D.; Zhang, C.; Barman, I. Towards Rational Design and Optimization of Near-Field Enhancement and Spectral Tunability of Hybrid Core-Shell Plasmonic Nanoprobes. *Sci. Rep.* **2019**, *9*, 16071. [CrossRef]
62. Agrawal, A.; Kriegel, I.; Milliron, D.J. Shape-Dependent Field Enhancement and Plasmon Resonance of Oxide Nanocrystals. *J. Phys. Chem. C* **2015**, *119*, 6227–6238. [CrossRef]
63. Lio, G.E.; Palermo, G.; De Luca, A.; Caputo, R. Tensile Control of the Thermal Flow in Plasmonic Heaters Realized on Flexible Substrates. *J. Chem. Phys.* **2019**, *151*, 244707. [CrossRef] [PubMed]
64. Ovejero, J.G.; Armenia, I.; Serantes, D.; Veintemillas-Verdaguer, S.; Zeballos, N.; López-Gallego, F.; Grüttner, C.; De La Fuente, J.M.; Puerto Morales, M.D.; Grazu, V. Selective Magnetic Nanoheating: Combining Iron Oxide Nanoparticles for Multi-Hot-Spot Induction and Sequential Regulation. *Nano Lett.* **2021**, *21*, 7213–7220. [CrossRef] [PubMed]

Disclaimer/Publisher's Note: The statements, opinions and data contained in all publications are solely those of the individual author(s) and contributor(s) and not of MDPI and/or the editor(s). MDPI and/or the editor(s) disclaim responsibility for any injury to people or property resulting from any ideas, methods, instructions or products referred to in the content.